Check for updates

High capacity all-solid-state lithium battery enabled by *in situ* formation of an ionic conduction path by lithiation of MgH$_2$†

Atsushi Inoishi, [ID] *[a] Hiroki Sato,[b] Yixin Chen,[b] Hikaru Saito,[a] Ryo Sakamoto, [ID] [a] Hikari Sakaebe [ID] [a] and Shigeto Okada [ID] [a]

All-solid-state Li batteries have attracted significant attention because of their high energy density and high level of safety. In a solid-state Li-ion battery, the electrodes contain a solid electrolyte that does not contribute directly to the capacity. Therefore, a battery that does not require a solid electrolyte in its electrode mixture should exhibit a higher energy density. In this study, a MgH$_2$ electrode was used as the negative electrode material without a solid electrolyte in its mixture. The resultant battery demonstrated excellent performance because of the formation of an ionic conduction path based on LiH in the electrode mixture. LiH and Mg clearly formed upon lithiation and returned to MgH$_2$ upon delithiation as revealed by TEM-EELS analysis. This mechanism of *in situ* electrolyte formation enables the development of a solid-state battery with a high energy density.

## Introduction

All-solid-state Li batteries have attracted significant attention because they can provide high energy densities and high levels of safety.[1,2] In recent years, sulfide- and oxide-based electrolytes have mainly been used in solid-state cells. However, hydride-based electrolytes are also well known for their high ionic conductivity and high compatibility with Li metal.[3,4] Several studies on the electrochemical formation of electrodes from electrolyte materials have recently been reported. Yamamoto *et al.* reported the *in situ* formation of an anode from a sodium superionic conductor (NASICON)-type solid electrolyte *via* electrochemical lithiation at 2.3 V *vs.* Li/Li$^+$, mainly *via* the redox reaction of Ti^{4+}/Ti^{3+}.[5] Han *et al.* reported a battery made from a single material using a Li$_{10}$GeP$_2$S$_{12}$ solid electrolyte to eliminate the high interfacial resistance of a solid-state battery.[6] Hakari reported all-solid-state batteries with Li$_3$PS$_4$ glass as an active material.[7,8] Our group recently studied an all-solid-state Li battery based on electrochemical Li$^+$ insertion into a Mg(BH$_4$)$_2$ anode; the battery exhibited a suitable operating voltage (0.9 V *vs.* Li/Li$^+$) and a large capacity.[9] The insertion of Li$^+$ into Mg(BH$_4$)$_2$ occurs *via* the following electrochemical reaction:

$$Mg(BH_4)_2 + 2Li^+ + 2e^- \rightarrow 2LiBH_4 + Mg \quad (1)$$
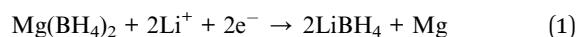
In this case, LiBH$_4$, a hydride with high Li$^+$ ionic conductivity, is generated and an ionic conduction path is formed during the electrochemical reaction. The LiBH$_4$ undergoes a structural transformation from a low-conductivity (orthorhombic) phase to a high-conductivity (hexagonal) phase at ~115 °C, and the high-temperature phase exhibits high Li$^+$ ionic conductivity.[10,11] Surprisingly, the electrode mixture does not require a solid electrolyte; reasonable battery performance was observed with an electrode composed of Mg(BH$_4$)$_2$ and acetylene black (AB) without LiBH$_4$ as an electrolyte. This performance is achieved *via* the *in situ* formation of an electrolyte, which contributes to an increase in the actual capacity of the battery. In a typical solid-state Li$^+$-ion battery, the electrodes contain a solid electrolyte and conductive carbon, which do not contribute directly to the battery's capacity; therefore, the new concept of *in situ* electrolyte formation enables the development of a battery with a high energy density. The reversible capacity of the Mg(BH$_4$)$_2$ electrode was found to be 563 mA h g^{-1} in a previous study.[9] However, the literature contains numerous reports on the electrochemical properties of Li batteries with hydride-based electrolytes and electrodes,[12–25] including MgH$_2$ electrodes, in particular.[12–22] The following electrochemical reaction occurs upon the insertion of Li$^+$ into MgH$_2$:

$$MgH_2 + 2Li^+ + 2e^- \rightarrow 2LiH + Mg \quad (2)$$
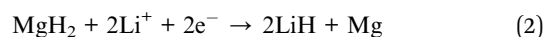
According to one report, a MgH$_2$ electrode demonstrated a reversible capacity of 1650 mA h g^{-1}.[12] In addition, the working potential of MgH$_2$ is ~0.5 V (*vs.* Li/Li$^+$), which provides an adequate margin from the potential of Li metal. Therefore, from the viewpoint of capacity and potential, MgH$_2$ has a large

[a] Institute for Materials Chemistry and Engineering, Kyushu University, Kasuga-koen 6-1, Kasuga 816-8580, Japan. E-mail: inoishi@cm.kyushu-u.ac.jp

[b] Interdisciplinary Graduate School of Engineering Sciences, Kyushu University, Kasuga-Koen 6-1, Kasuga-shi, Fukuoka 816-8580, Japan

advantage as an electrode material. MgH_2 is transformed into LiH upon insertion of Li^+ ions. Although the ionic conductivity of LiH is not as high as that of $LiBH_4$, LiH is a Li^+ ionic conductor.[26–28] Therefore, a MgH_2 electrode can undergo *in situ* electrolyte formation upon the insertion of Li^+ ions. Because the theoretical capacity of MgH_2 (2036 mA h g^{-1}) is much larger than that of $Mg(BH_4)_2$ (992 mA h g^{-1}), which was previously studied as an electrode material that forms an electrolyte *in situ*, MgH_2 should be a promising electrode material without a solid electrolyte incorporated into the electrode mixture. In the present study, the electrochemical *in situ* formation of a Li^+ ionic conduction path in MgH_2 is investigated and transmission electron microscopy with electron energy-loss spectroscopy (TEM-EELS) analysis is used to visualize the formation of the LiH and Mg in the electrode mixture during the electrochemical reactions.

Experimental

All operations were carried out in a glove box filled with Ar gas. Commercially available $LiBH_4$ (≥95%, Sigma-Aldrich) was hand milled for 5 min before use. The $LiBH_4$ was used as a solid electrolyte. Two composite powders containing MgH_2 (95%, Sigma-Aldrich) were prepared by a mechanical milling method: one containing a solid electrolyte and the other without the solid electrolyte. A planetary-type mill (FRITSCH Pulverisette 6) was used for mechanical milling. The composite powders were obtained by the mechanical milling of MgH_2 with $LiBH_4$ and AB in a 40 : 30 : 30 mass ratio or MgH_2 and AB in a 70 : 30 mass ratio at 400 rpm for 30 min. For the electrode without $LiBH_4$, other compositions (MgH_2 : AB = 99 : 1 and 95 : 5) were also evaluated. A cell set with a sleeve made of polyether ether ketone (PEEK, EQ-PSC, AA Portable Power Corp.) was used to fabricate a battery with an inside diameter of 10 mm. $LiBH_4$ was pressed at 255 MPa. A portion of either the MgH_2 + $LiBH_4$ + AB or MgH_2 + AB mixture was placed on top of the $LiBH_4$ layer and pressed at 320 MPa. Li foil (Honjo Metal Co.) was pressed by hand between an SUS plate and a $LiBH_4$ electrolyte layer as a counter electrode. Herein, batteries with a structure of Li/$LiBH_4$/MgH_2 + $LiBH_4$ + AB (40 : 30 : 30 by weight) and Li/$LiBH_4$/MgH_2 + AB (70 : 30, 95 : 5, 99 : 1 by weight) were prepared. The discharge/charge properties of the batteries were examined using a galvanostat (Hokuto Denko Co.) at a current density of 0.5 mA cm^{-2} and at 120 °C. The voltage range was set between 0.3 and 1.0 V (*vs.* Li/Li^+). The capacity was calculated using two methods. First, the capacity of each device was calculated on the basis of the mass of MgH_2 in the electrode mixture, not including the masses of the solid electrolyte and AB. Second, the capacity was calculated from the mass of the electrode mixture including MgH_2, the solid electrolyte, and the AB. Scanning Electron Microscope (SEM) images were obtained by JCM-7000 (JEOL Ltd). Nanoscopic structural analysis was performed using transmission electron microscopy (Titan Cubed 60-300 G2, Thermo Fisher Scientific) with a monochromator for the electron source, a spherical aberration corrector (DCOR, CEOS) for the probe-forming lens system, detectors for energy-dispersive X-ray spectroscopy (Super X), and an energy filter for electron

energy loss spectroscopy (EELS; GIF Quantum 965 spectrometer, Gatan). The microscope was operated in scanning transmission electron microscopy (STEM) mode at an accelerating voltage of 300 kV. Three samples were prepared for the STEM analysis: MgH_2 and AB composite powders in their initial state, and the corresponding layer in the charged and discharged states. These samples were extracted from the batteries and were mechanically crushed in a glove box filled with Ar gas. The resultant submicrometer grains were dispersed onto TEM grids with a carbon supporting film and were loaded into a dedicated cryo-holder (Mel-Build) for transfer from the glove box to the transmission electron microscope without exposure to the atmosphere. During the STEM analysis, the temperature at the top end of the sample holder was maintained at −100 °C by liquid N_2.

Results and discussion

Fig. 1 shows schematics of the solid-state battery without a $LiBH_4$ solid electrolyte in the electrode mixture. A solid electrolyte is typically required in the electrode mixture; however, the electrode reaction can be promoted by the *in situ* formation of a LiH solid electrolyte. In the case of the MgH_2 electrode, LiH is formed during lithiation. If the conductivity of LiH is sufficiently high, the electrochemical reaction is considered to proceed over the entire electrode mixture (Fig. 1). Initially, the formation of LiH and Mg will proceed from the interface between the solid electrolyte layer and the electrode mixture and the electrode reaction will proceed toward the current collector through the LiH to form an ionic conduction pathway. In the present study, the electrochemical properties of cells with and without the $LiBH_4$ solid electrolyte in the electrode mixture were compared. The morphology of the electrode mixture (MgH_2 : AB = 70 : 30) was compared using scanning electron microscopy (SEM) observations (ESI, Fig. S1†). Before the observations, the powder samples were pressed at 320 MPa, which is the same pressure used to construct the solid-state batteries. An SEM micrograph and energy-dispersive X-ray (EDS) mapping images (magnification: 3000×) of the electrode mixture are shown in Fig. S1(a) and S2(b),† respectively. The results confirm that AB particles with sizes of ∼0.5 μm were uniformly dispersed on the sample surfaces. Fig. S1(c)† shows an SEM image at higher magnification (100 00×). Numerous 2–3 μm wide regions with a high density were observed, along with
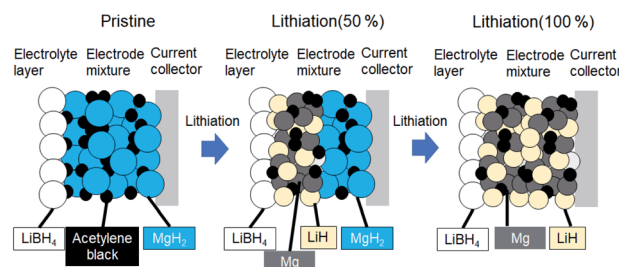

Fig. 1 Schematics of electrochemical reactions of solid–state battery with MgH_2 electrode.

© 2022 The Author(s). Published by the Royal Society of Chemistry

a large number of grain boundaries, indicating that the density after pelletization was not high. Fig. 2a and b show the discharge–charge curves for the Li/LiBH$_4$/MgH$_2$ cell with and without LiBH$_4$ in the electrode mixture, respectively. For the cell with LiBH$_4$ in the electrode mixture, the initial lithiation and delithiation capacities were 1738 and 1685 mA h g^{-1}, respectively. These capacities are similar to those previously reported.[12] However, for the electrode mixture without LiBH$_4$, the initial capacity was 1818 mA h g^{-1} and increased to 1885 mA h g^{-1} in the second cycle. The difference in cell voltage between the first charge and first discharge (at 50 mA h g^{-1}) with and without LiBH$_4$ was 60 mV and 53 mV, respectively. Surprisingly, these results suggest that similar performance can be achieved in the cell without LiBH$_4$ in the electrode mixture. Fig. 3 shows annular dark field (ADF) STEM images, EELS spectra, and energy-filtered maps obtained from the initial MgH$_2$ and AB composite powders (Fig. 3a–f), the powders in the discharged state (Fig. 3g–m), and the powders in the charged state (Fig. 3n–r). For the initial state, several plasmon peaks were observed in valence EELS (VEELS) spectra collected from different areas (Fig. 3b). A plasmon peak was detected at 14.5 eV for a large fraction of the observed particles, as shown in

a typical spectrum (red spectrum in Fig. 3b); an L-edge of Mg was also detected at 52.5 eV in the spectrum corresponding to the same area (Fig. 3c). The plasmon peak energy and the shape of the energy-loss near-edge structure (ELNES) at the Mg L-edge agree well with EELS and X-ray Raman scattering (XRS) spectra previously reported for MgH$_2$.[29–31] AB particles were also identified on the basis of π plasmon and π + σ plasmon peaks observed at 6.5 eV and 27 eV, respectively. These plasmon peaks are specific to graphite-like materials.[32,33] For the discharged states (lithiated state), two plasmon peaks were detected at 10.6 eV and 15 eV; these peaks appear in different areas in the energy-filtered maps (Fig. 3j and k). The peak at 10.6 eV originates from metallic Mg,[29,30] as also supported by the Mg map obtained by EDS (Fig. S2†). The peak at 15 eV indicates the existence of LiH, and is also supported by the ELNES results at the Li K-edge (Fig. 3i). The plasmon peak energy and the shape of the ELNES agree well with EELS or XRS spectra reported for LiH in previous studies.[34,35] A Li K-edge was also detected in another area not assigned to either metallic Mg or LiH (Fig. 3i). However, the shape of the corresponding ELNES differs dramatically from those for LiH and other Li compounds;[34] in addition, the plasmon peak energy and shape also differ from those for LiH (Fig. 3h). EDS analysis indicates that the surface of the particles includes a larger amount of oxygen relative to the LiH area inside the particle (Fig. S3†), suggesting that the surface was oxidized by residual O$_2$ gas or vapor after the sample was crushed. For the charged state (delithiated state), a plasmon peak and an L-edge of Mg were again detected at 14.5 eV and 52.5 eV (Fig. 3o and p). The obtained spectra fully reproduce those of the initial state; that is, MgH$_2$ particles were generated during the charge process. Accordingly, the STEM-EELS analysis supports the proposed concept of an electrochemical reaction that includes *in situ* electrolyte formation during discharge–charge cycling. We found that the MgH$_2$ electrode does not require that a LiBH$_4$ solid electrolyte be incorporated into the electrode mixture because LiH is formed during Li$^+$ insertion. In industrial applications, reducing the amount of carbon is also important for increasing the actual capacity of the electrode. We therefore attempted to decrease the amount of carbon in the electrode mixture (Mg + AB). Fig. S3† shows the discharge–charge curves for cells with different amounts of AB. Surprisingly, even for the composition MgH$_2$: AB = 99 : 1, the discharge–charge reaction proceeded at 0.5 mA cm^{-2}. When the current density was lowered to 0.05 mA cm^{-2}, a lithiation capacity of 1268 mA h g^{-1} was observed even for the electrode with a composition of MgH$_2$: AB = 99 : 1. However, the capacity decreased with decreasing AB content. Assuming that the density of carbon is 2 g cm^{-3}, the volume percentages of carbon at MgH$_2$: AB = 70 : 30 and 99 : 1 are 15.8% and 1.5%, respectively. Therefore, when the low-carbon-content electrode (MgH$_2$: AB = 99 : 1) was used, the electron conduction path was not well connected. Fig. 4a shows the discharge–charge curve for the "actual capacity" on the *x*-axis. Here, "actual capacity" refers to the capacity per weight of the whole electrode mixture, including the carbon, active material, and the solid electrolyte. The actual lithiation capacity without LiBH$_4$ (MgH$_2$: AB = 70 : 30) was more than twice as large as the
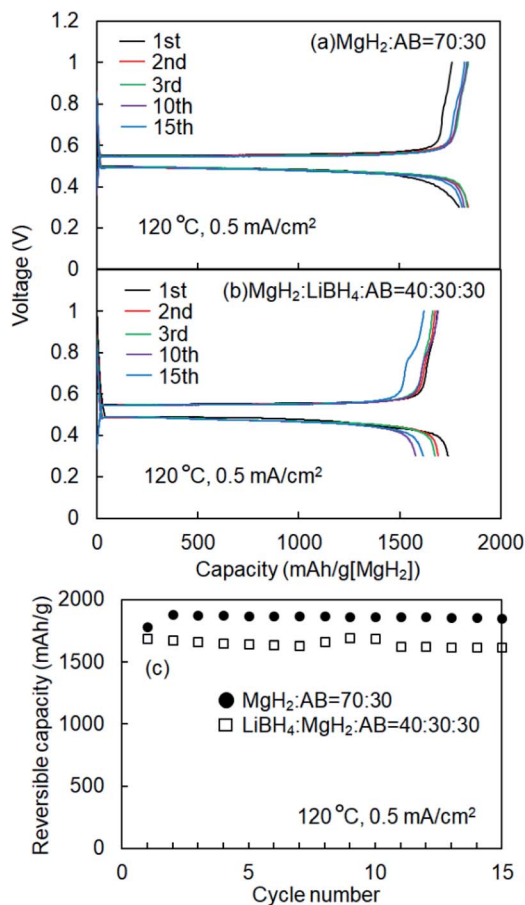

Fig. 2 (a) Discharge–charge curves for Li/LiBH$_4$/MgH$_2$ cell without LiBH$_4$ in electrode mixture. (b) Charge–discharge curves for Li/LiBH$_4$/MgH$_2$ cell with LiBH$_4$ in electrode mixture. (c) Cyclic properties of Li/LiBH$_4$/MgH$_2$ cell with and without LiBH$_4$ in electrode mixture.
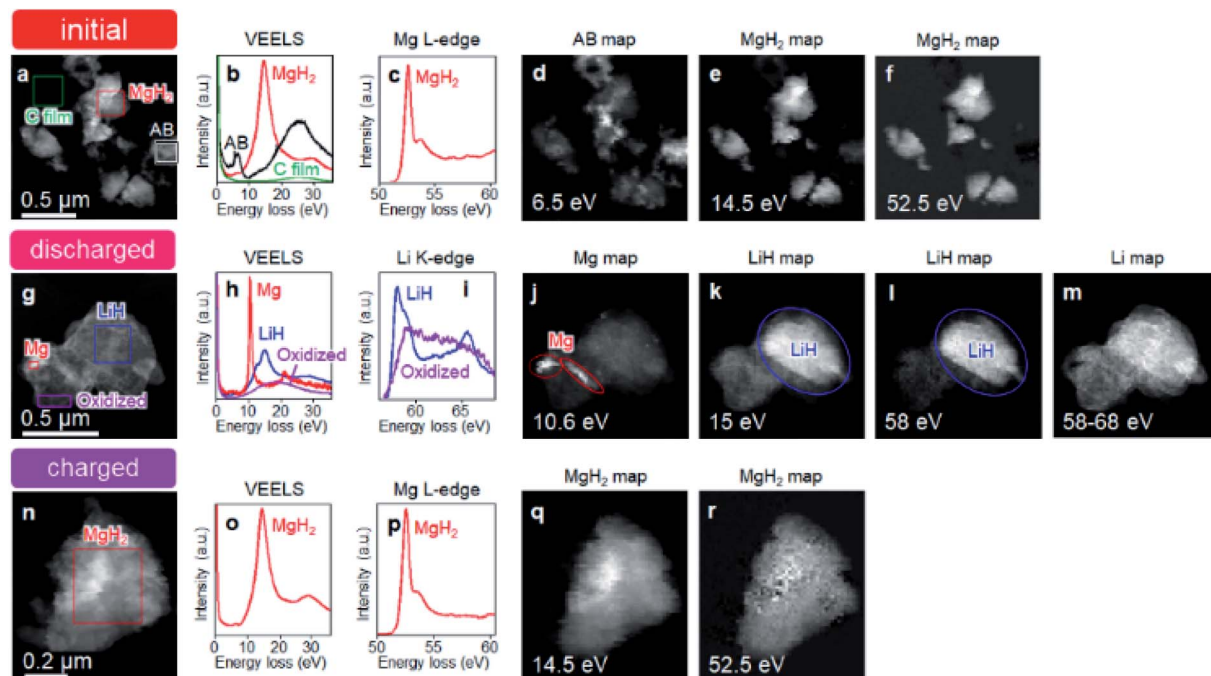
Fig. 3 STEM-EELS analysis of initial MgH$_2$ and AB composite powders, discharged state, and charged state. (a) ADF-STEM image of initial MgH$_2$ and AB composite powders. (b and c) Typical VEELS spectra and ELNES at Mg L-edge extracted from areas indicated in (a). The colour of the selection windows in (a) corresponds to the colour used for plotting each of the spectra in (b) and (c). (d–f) Energy-filtered maps of (a) at (d) 6.5 eV, (e) 14.5 eV, and (f) 52.5 eV. (g) ADF-STEM image of composite powders in discharged state. (h and i) Typical VEELS spectra and ELNES at Li K-edge extracted from areas indicated in (g). The colour of the selection windows in (g) corresponds to the colour used for plotting each of the spectra in (h) and (i). (j–m) Energy-filtered maps corresponding to (g) at (j) 10.6 eV, (k) 15 eV, (l) 58 eV, and (m) 58 to 68 eV. (n) ADF-STEM image of composite powders in charged state (after first discharge–charge cycle). (o and p) Typical VEELS spectrum and ELNES at Mg L-edge extracted from area indicated in (n). (q and r) Energy-filtered maps corresponding to (n) at (j) 14.5 eV and (m) 52.5 eV. The energy width for filtering in all the maps except that in (m) is 1 eV, where the aforementioned energy values for the maps are at the centers of the selected energy ranges of the 1 eV width. The plotted intensity in each of the energy-filtered maps was normalized by the intensity of the zero-loss peak so that it was proportional to the excitation probability.

capacity with LiBH$_4$ (LiBH$_4$: MgH$_2$: AB = 40 : 30 : 30). However, the actual Li insertion capacity was approximately the same when the current density was 0.05 mA cm^{-2} at MgH$_2$: AB = 99 : 1 and when the current density was 0.5 mA cm^{-2} at MgH$_2$: AB = 70 : 30. Fig. 4b shows the discharge–charge efficiency in the initial cycle and the utilization efficiency of the

MgH$_2$ in the initial discharge capacity in the cell with a different electrode composition. The charge–discharge efficiency increased with increasing carbon content. When the carbon content was low, the reversible capacity was drastically diminished. We speculate that, when a large discharge (lithiation) capacity cannot be attained, the charge (delithiation) capacity
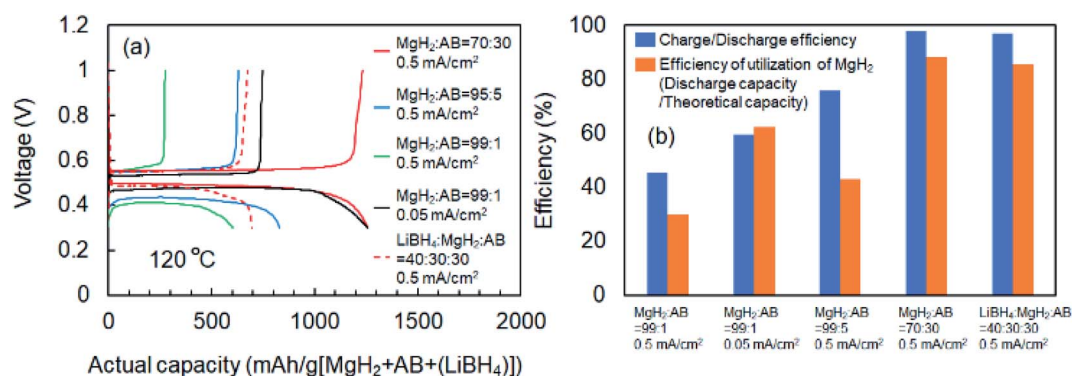

Fig. 4 (a) Discharge (lithiation)–charge (delithiation) curves for cells with different electrode compositions. (b) Discharge (lithiation)–charge (delithiation) efficiency in initial cycle and utilization efficiency of initial discharge capacity in cells with different electrode compositions. Results were obtained for different electrode mixture compositions and different current densities during discharge–charge measurements.

also decreases because sufficient ionic and electronic conduction paths are not formed in the electrode mixture. When the carbon content is low, a greater charge capacity (delithiation) can be attained in the second cycle than in the first cycle because the ionic and electronic conduction paths are gradually connected in the electrode mixture by cycling. The network of the ionic and electronic paths may change depending on the composition of the electrode mixture, current density, and the temperature. Details of the morphology of the electrode mixture will be revealed in a future study.

Conclusions

In summary, this work demonstrated the *in situ* formation of an ionic conducting path upon lithiation of MgH_2. The electrochemical performance of the cell without $LiBH_4$ in the electrode mixture matched that of the cell with $LiBH_4$ electrolyte incorporated. LiH and Mg clearly formed upon lithiation and returned to MgH_2 upon delithiation, as revealed by TEM-EELS analysis. Even when the composition was $MgH_2 : AB = 99 : 1$, the discharge–charge reaction proceeded. The electrochemical formation of LiH contributed to the superior electrochemical performance of the conversion reaction in the absence of an electrolyte in the electrode mixture. This concept of *in situ* electrolyte formation should be useful in designing novel high-capacity anodes for next-generation all-solid-state batteries.

Conflicts of interest

There are no conflicts of interest to declare.

Acknowledgements

Notes and references

1 O. Sheng, C. Jin, X. Ding, T. Liu, Y. Wan, Y. Liu, J. Nai, Y. Wang, C. Liu and X. Tao, *Adv. Funct. Mater.*, 2021, **31**, 2100891.

2 Z. Gao, H. Sun, L. Fu, F. Ye, Y. Zhang, W. Luo and Y. Huang, *Adv. Mater.*, 2018, **30**, 1705702.

3 K. Kisu, S. Kim, H. Oguchi, N. Toyama and S. Orimo, *J. Power Sources*, 2019, **436**, 226821.

4 S. Kim, H. Oguchi, N. Toyama, T. Sato, S. Takagi, T. Otomo, D. Arunkmar, N. Kuwata, J. Kawamura and S. Orimo, *Nat. Commun.*, 2019, **10**, 1081.

5 T. Yamamoto, Y. Sugiura, H. Iwasaki, M. Motoyama and Y. Iriyama, *Solid State Ionics*, 2019, **337**, 19–23.

6 F. Han, T. Gao, Y. Zhu, K. J. Gaskell and C. Wang, *Adv. Mater.*, 2015, **27**, 3473–3483.

7 T. Hakari, Y. Sato, S. Yoshimi, A. Hayashi and M. Tatsumisago, *J. Electrochem. Soc.*, 2017, **164**, A2804–A2811.

8 T. Hakari, M. Nagao, A. Hayashi and M. Tatsumisago, *J. Power Sources*, 2015, **293**, 721–725.

9 H. Sato, R. Sakamoto, H. Minami, H. Izumi, K. Ideta, A. Inoishi and S. Okada, *Chem. Commun.*, 2021, **57**, 2605–2608.

10 M. Matsuo, Y. Nakamori, S. Orimo, H. Maekawa and H. Takamura, *Appl. Phys. Lett.*, 2007, **91**, 224103–224105.

11 H. Maekawa, M. Matsuo, H. Takamura, M. Ando, Y. Noda, T. Karahashi and S. Orimo, *J. Am. Chem. Soc.*, 2009, **131**, 894–895.

12 L. Zeng, K. Kawahito, S. Ikeda, T. Ichikawa, H. Miyaoka and Y. Kojima, *Chem. Commun.*, 2015, **51**, 9773–9776.

13 S. Ikeda, T. Ichikawa, K. Kawahito, K. Hirabayashi, H. Miyaoka and Y. Kojima, *Chem. Commun.*, 2013, **49**, 7174–7176.

14 F. Cano-Banda, A. Gallardo-Guierrez, L. Luviano-Ortiz, A. Hernandez-Guerrero, A. Jain and T. Ichikawa, *Int. J. Hydrogen Energy*, 2021, **46**, 1030–1037.

15 L. Zeng, T. Ichikawa, K. Kawahito, H. Miyaoka and Y. Kojima, *ACS Appl. Mater. Interfaces*, 2017, **9**, 2261–2266.

16 L. Huang, L. Aymard and J. Bonnet, *J. Mater. Chem. A*, 2015, **3**, 15091–15096.

17 A. E. Kharbachi, H. Uesato, H. Kawai, S. Wenner, H. Miyaoka, M. H. Sørby, H. Fjellvåg, T. Ichikawa and B. C. Hauback, *RSC Adv.*, 2018, **8**, 23468–23474.

18 Y. Oumellal, A. Rougier, G. A. Nazri, J.-M. Tarascon and L. Aymard, *Nat. Mater.*, 2008, **7**, 916–921.

19 S. Brutti, G. Mulas, E. Piciollo, S. Panero and P. Reale, *J. Mater. Chem.*, 2012, **22**, 14531–14537.

20 S. Ikeda, T. Ichikawa, K. Goshome, S. Yamaguchi, H. Miyaoka and Y. Kojima, *J. Solid State Electrochem.*, 2015, **19**, 3639–3644.

21 D. Meggiolaro, G. Gigli, A. Paolone, P. Reale, M. L. Doublet and S. Brutti, *J. Phys. Chem. C*, 2015, **119**, 17044–17052.

22 Y. Oumellal, C. Zlotea, S. Bastide, C. Xachet-Vivier, E. Léonel, S. Sengmany, E. Leroy, L. Aymard, J. Bonnet and M. Latroch, *Nanoscale*, 2014, **6**, 14459–14466.

23 Y. Matsumura, K. Takagishi, H. Miyaoka and T. Ichikawa, *Mater. Trans.*, 2019, **60**, 2183–2187.

24 F. Mo, X. Chi, S. Yang, F. Wu, Y. Song, D. Sun, Y. Yao and F. Fang, *Energy Storage Mater.*, 2019, **18**, 423–428.

25 S. Sartori, F. Cuevas and M. Latroche, *Appl. Phys. A*, 2016, **122**, 135.

26 V. B. Ptashnik, T. Y. Dunaeva and Y. M. Baikov, *Phys. Status Solidi B*, 1982, **110**, K121–K124.

27 M. Ikeya, *J. Phys. Soc. Jpn.*, 1977, **42**, 168–174.

28 P. A. Varotsos and S. Mourikis, *Phys. Rev. B: Solid State*, 1974, **10**, 5220–5224.

29 B. Paik, I. P. Jones, A. Walton, V. Mann, D. Book and I. R. Harris, *Philos. Mag. Lett.*, 2010, **90**, 1–7.

30 M. Hamm, M. D. Bongers, V. Roddatis, S. Dietrich, K. H. Lang and A. Pundt, *Int. J. Hydrogen Energy*, 2019, **44**, 32112–32123.

31 C. J. Sahle, S. Kujawski, A. Remhof, Y. Yan, N. P. Stadie, A. Al-Zein, M. Tolan, S. Huotari, M. Krisch and C. Sternemann, *Phys. Chem. Chem. Phys.*, 2016, **18**, 5397–5403.

32 L. Calliari, S. Fanchenko and M. Filippi, *Carbon*, 2007, **45**, 1410–1418.

33 S. Urbonaite, S. Wachtmeister, C. Mirguet, E. Coronel, W. Y. Zou, S. Csillag and G. Svensson, *Carbon*, 2007, **45**, 2047–2053.

34 P. S. Miedema, P. Ngene, A. M. J. van der Eerden, D. Sokaras, T. C. Weng, D. Nordlund, Y. S. Au and F. M. F. de Groot, *Phys. Chem. Chem. Phys.*, 2014, **16**, 22651–22658.

35 M. J. Zachman, Z. Tu, S. Choudhury, L. A. Archer and L. F. Kourkoutis, *Nature*, 2018, **560**, 345–349.